Revision 2

Telescoped boiling and cooling mechanisms triggered hydrothermal stibnite precipitation: Insights from the world's largest antimony deposit in Xikuangshan China

Hao-Cheng Yu[1], Kun-Feng Qiu[1*], Adam C. Simon[2], Da Wang[1], Ryan Mathur[3], Ruo-Qi Wan[1], Xiang-Yong Jiang[1], Jun Deng[1]

[1] *State Key Laboratory of Geological Processes and Mineral Resources, School of Earth Sciences and Resources, China University of Geosciences, Beijing 100083, China*

[2] *Department of Earth & Environmental Sciences, University of Michigan, Ann Arbor, MI 48109, USA*

[3] *Department of Geology, Juniata College, Huntingdon, PA 16652, USA*

*Corresponding author

Dr. Kun-Feng Qiu

KunfengQiu@qq.com; ORCID: 0000-0002-3185-9446

Professor, China University of Geosciences, Beijing

No. 29 Xueyuan Road, Haidian District, Beijing, 100083, P.R. China

Abstract

Society annually consumes 250% more Sb relative to the year 1960 and a sustainable supply of antimony depends critically on understanding the precipitation mechanism of stibnite (Sb_2S_3) that is the globally predominant source of this important technology metal. Previous solubility studies revealed that antimony is transported in mesothermal hydrothermal fluids mainly as thioantimonite ($H_2Sb_2S_4$, $HSb_2S_4^-$, $Sb_2S_4^{2-}$) and hydroxothioantimonite ($Sb_2S_2(OH)_2$). Thioantimonite can transform to hydroxothioantimonite as the decline of H_2S concentration. However, whether this transition occurs in hydrothermal systems and its role in stibnite precipitation are unknown. In this work, bulk Sb isotope measurements for stibnite from the world's largest Sb deposit in Xikuangshan China were conducted to address ore fluid evolution and stibnite precipitation mechanisms. The abundance of the stable antimony isotopes ^{121}Sb and ^{123}Sb were measured in stibnite from the Xikuangshan orebodies and reported as $\delta^{123}Sb$. The $\delta^{123}Sb$ values show a trend of decreasing first and then increasing from proximal to distal parts of orebodies. This reveals that ^{123}Sb had been preferentially partitioned from the ore fluid into stibnite first, then ^{123}Sb remained preferentially dissolved in the ore fluid. These data indicate that the dominant Sb-complex transforms to $Sb_2S_2(OH)_2$ from $H_2Sb_2S_4$ with consuming of H_2S. Speciation diagram considerations indicate that stibnite precipitation from the ore fluid was controlled by two telescoped processes: 1) boiling of the ore fluid induced a decrease in H_2S that reduced the solubility of $H_2Sb_2S_4$, and 2) subsequent cooling that induced a decrease in the solubility of $Sb_2S_2(OH)_2$. This study highlights that understanding the controls of Sb isotope fractionation is critical to constrain fluid evolution and stibnite precipitation mechanisms in Sb-rich mineral systems. In particular, the stable Sb

43 complex in the hydrothermal ore fluid may change during fluid evolution and affect the
44 isotope fractionation mechanism.
45
46 **Keyword:** Sb isotope; stibnite precipitation; boiling; cooling; Xikuangshan Sb deposit
47

48 **1. Introduction**

49 Antimony is a critical mineral commodity essentially for a wide variety of products
50 including flame retardants and alloys for batteries, plain bearings, and solders (Schulz et al.,
51 2018). This metal is found in more than 100 minerals in a variety of deposits. The most
52 common antimony ore mineral is stibnite (Sb_2S_3) occurring as fault-controlled or strata-
53 bound orebodies (Hofstra et al., 2013; Xie, 2018; Fu et al., 2020d). Simple stibnite-bearing
54 quartz ± carbonate veins account for most of the current and recent mine production.
55 Antimony resources are unevenly distributed globally (Fig. 1). The majority of identified Sb
56 resources are located in China who leads global production (Schulz et al., 2018; Yu et al.,
57 2022). Society annually consumes 250 % more Sb relative to the year 1960, while the
58 antimony production continued to decline (Schulz et al., 2018). A sustainable supply of
59 antimony depends critically on understanding the ore fluid evolution and stibnite
60 precipitation mechanisms in hydrothermal Sb deposits.

61 Antimony displays a wide range of oxidation states (Sb^{3-} to Sb^{5+}), most of which are
62 present in trivalent and pentavalent forms in crustal fluids (Zotov et al., 2003; Fu et al.,
63 2020d). Under surface oxidizing conditions, Sb^{5+} may be predominant, and Sb-bearing
64 hydrothermal fluids mainly contain Sb^{3+} (Fu et al., 2020d). In hydrothermal fluids, Sb is
65 transported mainly as thioantimonite ($H_2Sb_2S_4$, $HSb_2S_4^-$, $Sb_2S_4^{2-}$), hydroxothioantimonite

66 ($Sb_2S_2(OH)_2^0$), hydroxide complexes ($Sb(OH)_2^+$, $Sb(OH)_3^0$, and $Sb(OH)_4^-$), chloride
67 complexes, and carbonate or bicarbonate species (Krupp, 1988; Hagemann and Luders,
68 2003; Zotov et al., 2003; Wilson et al., 2007; Fu et al., 2020d). Given that (1) hydroxide
69 complexes are formed in sulfur-free system, (2) chloride complexes are unimportant in
70 antimony speciation except in extremely acid, chloride-rich solutions, and (3) carbonate or
71 bicarbonate species are unimportant in antimony transport, thioantimonite and
72 hydroxothioantimonite are thus likely to be dominant in ore fluids (Krupp, 1988; Williams-
73 Jones and Norman, 1997). In mesothermal ore fluids, solubility experimental studies
74 revealed the distribution of antimony species as a function of pH. Hydroxothioantimonite
75 controls antimony transport at acidic pH, and thioantimonite is dominant at intermediate to
76 alkaline pH (Krupp, 1988). In addition, the solubility experimental studies indicated that
77 $H_2Sb_2S_4$ can transform to $Sb_2S_2(OH)_2$ with the consuming of H_2S (Krupp, 1988; Zotov et al.,
78 2003). Previous research showed that different processes can decrease the solubility of
79 corresponding Sb complexes in aqueous hydrogen sulfide solutions, e.g., consuming of H_2S
80 can induce the stibnite precipitation from thioantimonite, while decreasing temperature can
81 decrease the solubility of both thioantimonite and hydroxothioantimonite (Krupp, 1988;
82 Zotov et al., 2003). Both pH change and cooling have been shown to be the causes of
83 stibnite deposition in geothermal power stations in New Zealand (Wilson et al., 2007).
84 Numerous fluid inclusion studies have been carried out on hydrothermal Sb-rich deposits
85 and proposed various models proposed for the major geological processes, including fluid
86 cooling, fluid boiling, fluid mixing, and fluid-rock interaction (Hagemann and Luders, 2003;
87 Su et al., 2009; Muntean et al., 2011; Hu and Peng, 2018; Xie, 2018; Deng et al., 2020b; Fu
88 et al., 2020c; Qiu et al., 2020; Voisey et al., 2020; Wu et al., 2021; Yu et al., 2021). These

studies inferred these geological processes decrease the solubility of Sb complexes and control stibnite precipitation. It's clear that the concentration of H_2S will change with the precipitation of stibnite, likely inducing the transition of dominant Sb complexes. However, none of these studies focus on the transition of dominant Sb complexes as fluid evolution and explore its role in stibnite precipitation.

Several studies have underpinned the crucial importance of metal isotope tracing as a prerequisite to constrain the evolution of large-scale ore-forming systems (Mathur et al., 2005; Toutain et al., 2008; Kelley et al., 2009; Qiu et al., 2017; Gao et al., 2018; Mathur et al., 2018; Ohmoto, 2018; Zhu et al., 2018; Li et al., 2019; Wang et al., 2020a; Yu et al., 2020). The application of the Sb isotope system as a process tracer for ore deposits is in its infancy (Rouxel et al., 2003; Zhai et al., 2021). Although the dominant Sb species involved and their associated isotope fractionations are poorly understood, initial studies explored the range of Sb isotope compositions for natural samples (Rouxel et al., 2003; Wen et al., 2018; Kaufmann et al., 2021), fractionation mechanisms (Lobo et al., 2012; Resongles et al., 2015; Wen et al., 2018), and mineralization processes (Zhai et al., 2021). Reduction processes from Sb^{5+} to Sb^{3+} exert a strong fractionation of 0.9 ‰ (Rouxel et al., 2003). Lighter Sb isotopes preferentially partition into the Sb^{3+} phase, whereas heavier Sb isotopes remain in the Sb^{5+} phase (Rouxel et al., 2003). Additionally, Sb isotope fractionation can be caused by evaporation and precipitation of Sb during Sb-containing waste combustion and Sb ore smelting (Tanimizu et al., 2011). Zhai et al. (2021) proposed that separation of stibnite from an Sb-bearing fluid related to reaction kinetics as a cause for Sb isotope fractionation. These studies demonstrate that the Sb isotope have the potential to be used as a process tracer for the fluid evolution of large Sb ore systems.

112 The Xikuangshan deposit in Hunan Province, China, is the world's largest Sb deposit,
113 which has supplied more than half of all globally mined Sb (Yang et al., 2006; Deng and
114 Wang, 2016; Hu et al., 2017; Goldfarb et al., 2019; Fu et al., 2020a; Luo et al., 2020). It
115 provides a natural case to better understand the ore fluid evolution and stibnite precipitation
116 mechanisms in hydrothermal Sb deposits. In this study, we report δ^{123}Sb isotope values for
117 stibnite from the proximal steeply-dipping orebodies. This new dataset can be compared
118 with existing δ^{123}Sb isotope values from the distal shallowly-dipping orebodies to address ore
119 fluid evolution and stibnite precipitation mechanisms.
120
121 **2. Geology of the Xikuangshan Sb deposit**
122 The Xiangzhong province of China hosts the world's largest Sb reserves in the world,
123 with over 171 known antimony mineral deposits and 2.7 Mt Sb reserves (Deng et al., 2017;
124 Hu and Peng, 2018; Wang et al., 2020b; Fu et al., 2022; Yan et al., 2022). Estimates of
125 historic mining activity indicate that approximately 1 Mt of Sb have been produced from the
126 Xikuangshan Sb deposit beginning in the 16th century and pre-mining reserves are 2.5 Mt at
127 an average Sb grade of 4.0 wt. % (Fu et al., 2020c). The Sb resource of the deposit is mined
128 by four mines, referred to as Laokuangshan and Tongjiayuan mines in the North Ore Block
129 and Wuhua and Feishuiyan mines in the South Ore Block (Fig. 2A). The mining area is
130 dominated by Middle Devonian to Lower Carboniferous carbonate rocks and minor shale,
131 which is locally interbedded with siltstone and argillite and formed a NE- striking anticline.
132 An Early Cretaceous (127.8 Ma; biotite K-Ar) lamprophyre dike aligned in the NE direction
133 was emplaced into the strata in the eastern part of the mine (Wu and Hu, 2000). It exhibits a
134 calc-alkaline affinity, with geochemical signatures implying it was derived from enriched

lithospheric mantle (Xie et al., 2001; Hu and Peng, 2018). A series of broadly parallel NE-striking normal faults crosscut the mine and were cut by later NW-striking strike-slip faults (Fig. 2A).

Much of the Sb resource in the Xikuangshan deposit is hosted in the footwall of the NE-striking fault F75. It hosts three types of orebodies: (1) steeply-dipping orebodies along the footwall of the major deep-seated fault F75, (2) shallowly-dipping orebodies within the strata controlled by a NE- striking anticline, and (3) transitional zones between the steeply-dipping and shallowly-dipping orebodies (Fig. 2B). All of the three types of orebodies show a southward plunge, leading to a relatively deeper mining depth in the South Ore Block of the Xikuangshan deposit. The ore-bearing zones are commonly hosted within the Devonian silicified limestone (Fig. 3). Hydrothermal alteration of the three types of orebodies is similar in appearance and mineral assemblages. It is characterized by quartz alteration and carbonate alteration (Figs. 3A, 3C, 4A), as well as local fluorite alteration. Ores in the Xikuangshan deposit are divided into quartz-stibnite and calcite-quartz-stibnite vein-style mineralization and disseminated minor barite-quartz-stibnite and fluorite-quartz-stibnite veinlet-style mineralization around the vein-style mineralization (Fig. 4). In general, the shallowly-dipping orebodies are dominated by the quartz-stibnite ores (Fig. 4C), while the steeply-dipping orebodies are dominated by the calcite-quartz-stibnite ores (Fig. 4D). Optical microscopic investigation revealed that stibnite is the dominant sulfide mineral, with quartz, calcite, fluorite, and barite as gangue minerals (Fig. 5). Stibnite crystals from the shallowly-dipping and steeply-dipping orebodies are identical in mineralogy assemblages. Their size varies largely, ranging from tens of microns to several centimeters. Most of them are anhedral, growing along the margin of the quartz and calcite (Fig. 5A-C). Euhedral

158 needle-shaped crystals in limestone wall rock and calcite grains are also visible (Figs. 4B,
159 5D). Detrital zircons separated from the altered host rocks from the Xikuangshan deposit
160 yielded (U-Th)/He ages ranging from 156 to 117 Ma, constraining the antimony event to
161 late Mesozoic (Fu et al., 2020a). Microthermometry data for fluid inclusions hosted in
162 stibnite from both types of orebodies reveal similar ore fluid conditions. The
163 homogenization temperatures of stibnite from the shallowly-dipping orebodies range from
164 105 to 305 °C (averaging at 194 °C), with an average salinity of 6.0 wt.% NaCl equiv. For
165 fluid inclusions within stibnite in the steeply-dipping orebodies, their homogenization
166 temperatures range from 163 to 218 °C (averaging at 192 °C) with an average salinity of 8.1
167 wt.% NaCl equiv. (Lin, 2014; Hu and Peng, 2018; Zhang, 2018). Integrated He-Ar-C-O-Sr
168 isotopic data indicate that the ore fluids are modified air-saturated meteoric water (Fu et al.,
169 2022). The concentrations of Sb in different types of rocks in the region and S isotope show
170 that most of the Sb was derived from the Neoproterozoic basement rocks (Fu et al., 2022;
171 Long et al., 2022).
172
173 **3. Sampling strategy and methods**
174 Zhai et al. (2021) measured Sb isotope abundances in stibnite sampled from the
175 shallowly-dipping orebodies and the transitional zones between the steeply-dipping and
176 shallowly-dipping orebodies. To further understand the ore fluid evolution and stibnite
177 precipitation mechanisms in the Xikuangshan deposit, the steeply-dipping orebodies are
178 sampled in this study. Twenty-six samples spanning all the main steeply-dipping orebodies
179 at different levels in the Feishuiyan mine at the Xikuangshan deposit were collected (Fig.

6A). Optical microscopic investigation of all samples indicated that no sulfide inclusions were present in the analyzed stibnite (Fig. 5).

Stibnite separation was done by using standard methods of concentration including crushing, heavy liquids, and magnetic separation at Beijing Precambrian Inc., Beijing, China. The purity of all stibnite concentrates was assessed microscopically prior to isotopic analysis to ensure they were monomineralic and not oxidized. Stibnite aliquot purities were commonly ≥ 99% and never < 95%. Antimony isotope compositions of the 26 samples were measured on a Thermo Scientific Neptune Plus MC-ICP-MS in low resolution mode, wet plasma using Ni cones at Pennsylvania State University. The full analytical procedures are provided in Zhai et al. (2021). Alfa Star verified acids were used and total blanks of these acids are certified at less than 0.01 ppb Sb. Approximately 30-50 mg of stibnite was dissolved for 18 hours in 15 ml telfon beakers containing 2 ml of aquaregia. Complete dissolution of materials was visually confirmed. Samples were diluted with 2 % nitric acid with 100 ppb NIST 3161 Sn internal standard. Mass bias was corrected using $^{124}Sn/^{116}Sn$ and samples were bracketed with NIST 3102a standard. One block of 35 ratios with on peak blank subtraction with an integration time of 12s was conducted as part of the measurement protocol. The mass of ^{123}Sb was set in the standard between 5-6 volts (solutions at 100 ppb), all measurements reported are within 20% matching of this voltage. The variation of the bracketing the standard throughout the run is considered the largest source of error and it varied 0.018 ‰ (2SD). The majority of the samples were duplicated and fall within the reported error (Table 1). At this moment no stibnite standards are reported as a means of QA/QC, thus a High Purity ICPMS standard which have been now measured over 15 times

was used. The internal stibnite standard yields δ^{123}Sb values of 0.336 ‰ and 0.338 ‰, which are consistent with the standard analyses of 0.31 ± 0.02 ‰ in Zhai et al. (2021).

4. Results and previous data

The Sb isotope compositions of stibnite from this study and from the study of Zhai et al. (2021) are shown in Fig. 6A and listed in Table 1. Previous 39 Sb isotope measurements from Xikuangshan Zhai et al. (2021) were conducted either using the same analysis procedures at Pennsylvania State University as these new data (1/39 analyses) or at Rutgers University (39/39 analyses) and Washington State University (1/39 analyses), where cross-checking of standards and identical samples allows direct comparison of isotope ratios of samples.

The δ^{123}Sb values for samples from the steeply-dipping orebodies in the Feishuiyan mine range from +0.483 to +0.988 ‰ and decrease systematically from deep (proximal) to shallow (distal) levels in the system. Stibnite from the -604 m, -468 m, -192 m, -142 m, and -106 m levels of the steeply-dipping orebody yielded averaged δ^{123}Sb values of +0.958 ‰ ± 0.086 ‰ (n=2), +0.767 ‰ ± 0.043 ‰ (n=6), +0.590 ‰ ± 0.091 ‰ (n=7), +0.559 ‰ ± 0.071 ‰ (n=6), and +0.534 ‰ ± 0.079 ‰ (n=5) (2σ), respectively (Fig. 6B; Table 1). Zhai et al. (2021) measured Sb isotope abundances in stibnite sampled from the shallowly-dipping orebodies in the Feishuiyan mine in the South Ore Block. The δ^{123}Sb values of stibnite sampled from the shallowly-dipping orebody range from +0.21 ‰ to +0.86 ‰, but show a systematical increase from proximal to distal ores in the system (Fig. 6B; Table 1). The shallowly-dipping orebodies and the transitional zones between the steeply-dipping and shallowly-dipping orebodies in the North Ore Block were also measured by Zhai et al.

(2021). Those authors reported the δ^{123}Sb values ranging from 0.30 ‰ to 0.62 ‰ at the transitional zones. Similar to the South Ore Block, stibnite from the shallowly-dipping orebodies in the North Ore Block show an increase from proximal to distal ores in the system, ranging from -0.27 ‰ to +0.70 ‰ (Fig. 6B; Table 1)

5. Antimony isotopic fractionation model

Some geological processes that may lead to the variation in δ^{123}Sb values of stibnite reported here and from Zhai et al. (2021) in the Xikuangshan deposit include 1) mixing of hydrothermal fluid with an external-derived fluid (e.g., meteoric water; Neyedley et al., 2017; Qiu et al., 2017) and 2) isotope fractionation during hydrothermal processes (e.g., redox change, ore precipitation; Moynier et al., 2017; Teng, 2017; Deng et al., 2020a; Wang et al., 2020a; Qiu et al., 2021). Given the extremely low Sb concentration in meteoric water, the effect of external-derived fluid mixing on the Sb isotopic composition in the ore system can be easily excluded. Likewise, unaltered host rocks show low Sb concentration (Fu et al., 2020b), implying that the fluid-rock interaction cannot modify the Sb isotopic composition of the system. Considering that the reduced sulfur complexes (thioantimonite and hydroxothioantimonite) are dominant agents for transporting Sb in the hydrothermal fluids in Xikuangshan, it follows that S and Sb could originate from the same source (Long et al., 2022). As evidenced by the relatively homogeneous δ^{34}S of stibnite (average of 8.0 ± 0.5 ‰, 2σ; Fu et al., 2020c; Long et al., 2022 and references therein), fluid mixing may not be the cause of variation in δ^{123}Sb values. The most reasonable explanation for the observed variation in δ^{123}Sb values of stibnite are isotope fractionation during hydrothermal processes.

This is the peer-reviewed, final accepted version for American Mineralogist, published by the Mineralogical Society of America.
The published version is subject to change. Cite as Authors (Year) Title. American Mineralogist, in press.
DOI: https://doi.org/10.2138/am-2022-8490. http://www.minsocam.org/

A few studies explored possible causes of Sb isotopic fractionation in natural and experimental settings by assessing the effects of redox reactions (Rouxel et al., 2003; Kendall et al., 2017; Moynier et al., 2017) and kinetic Rayleigh fractionation (Watkins et al., 2017; Wang et al., 2020a; Zhai et al., 2021). Rouxel et al. (2003) reported the significant Sb isotopic fractionation of up to 0.9 ‰ in aqueous solutions during reduction of Sb^{5+} to Sb^{3+} in two duplicate experiments. The effect of reduction on the observed variation of $\delta^{123}Sb$ values in stibnite samples can be eliminated, considering that Sb^{3+} is the predominant ion species in Sb-bearing hydrothermal fluids and Sb^{5+} mostly exist in surficial environments (Zotov et al., 2003; Fu et al., 2020d). We propose that the systematic variability of $\delta^{123}Sb$ values in stibnite in the Xikuangshan orebodies are best explained by Rayleigh fractionation during the precipitation of stibnite from hydrothermal fluids. Rayleigh fractionation has been demonstrated to be a potential factor that can lead to metal isotope fractionation of, for example, copper (e.g., Gregory and Mathur, 2017), iron (e.g., Wang et al., 2018; Zhu et al., 2018; Zhang et al., 2021), molybdenum (e.g., Hannah et al., 2007; Li et al., 2019), zinc (e.g., Mondillo et al., 2018), cadmium (e.g., Wen et al., 2016; Zhu et al., 2017), and lead (e.g., Gao et al., 2018) during the precipitation of sulfide minerals from hydrothermal fluids in types of mineral systems. The Rayleigh fractionation model for Sb is illustrated in Fig. 6B as determined by using the equations

$$\delta^{123}Sb_{Fl}^{F} = (\delta^{123}Sb_{Fl}^{F=1} + 10^3) \times F^{\alpha-1} - 10^3 \quad (1)$$

$$\delta^{123}Sb_{S} = (\delta^{123}Sb_{Fl} + 10^3) \times \alpha - 10^3 \quad (2)$$

where Fl = ore-forming fluid, S = stibnite, $\delta^{123}Sb_{Fl}^{F=1}$ = initial Sb isotopic compositions, F = the fraction of reactant remaining, α = fractionation factor. We use subscript 1 (F_1, S_1, α_1)

This is the peer-reviewed, final accepted version for American Mineralogist, published by the Mineralogical Society of America.
The published version is subject to change. Cite as Authors (Year) Title. American Mineralogist, in press.
DOI: https://doi.org/10.2138/am-2022-8490. http://www.minsocam.org/

for the steeply-dipping orebody and transitional zone and subscript 2 (F_2, S_2, α_2) for the shallowly-dipping orebody in the fractionation equations.

An Sb isotope fractionation model for the steeply-dipping and shallowly-dipping orebodies is constructed by integrating the new data reported here and data in Zhai et al. (2021) (Fig. 6). For the shallowly-dipping orebodies, an initial δ^{123}Sb value ($\delta^{123}Sb_{S2}^{F2=1}$) of -0.16 ‰ ± 0.03 ‰ for stibnite is used based on the average δ^{123}Sb value of stibnite from the most proximal samples of the shallowly-dipping orebodies. A final $\delta^{123}Sb_{S2}^{F2=0}$ value of 0.85 ‰ ± 0.01 ‰ for stibnite is used to model the most distal samples of the shallowly-dipping orebodies. The fractionation factor α_2 is calculated as 0.99978 ± 0.00001. The initial δ^{123}Sb value of the ore fluid ($\delta^{123}Sb_{Fl2}^{F2=1}$) that precipitated the shallowly-dipping orebodies is thus calculated as 0.060 ‰ ± 0.011 ‰. Given that the hypogene ore-forming fluid ascended along the major fault F75 and stibnite precipitated first from that fluid within the steeply-dipping orebody and subsequently in the shallowly-dipping stratigraphically controlled orebodies, we use a final δ^{123}Sb value of 0.060 ‰ ± 0.011 ‰ for the ore fluid ($\delta^{123}Sb_{Fl1}^{F1=0.34}$) in the steeply-dipping orebodies. As the average δ^{123}Sb values from the deepest and shallowest ore samples are 0.958 ‰ and 0.490 ‰, the initial and final δ^{123}Sb values ($\delta^{123}Sb_{S1}^{F1=1}$ and $\delta^{123}Sb_{S1}^{F1=0}$) of stibnite in the steeply-dipping orebodies are calculated to be 0.960 ‰ ± 0.029 ‰ and 0.493 ‰ ± 0.002 ‰. The fractionation factor α_1 and the initial δ^{123}Sb value of the ore fluid ($\delta^{123}Sb_{Fl1}^{F1=1}$) are calculated to be 1.00043 ± 0.00003 and 0.530 ‰ ± 0.016 ‰, respectively (Fig. 6B).

6. Fluid evolution and precipitation mechanisms of ores

292 Rayleigh fractionation modeling of Sb isotopic compositions from the steeply- and
293 shallowly-dipping orebodies in the Xikuangshan deposit reveals opposite trends in $\delta^{123}Sb$
294 values during stibnite precipitation (Fig. 6B). This result is consistent with a difference in the
295 dominant Sb-complex dissolved in the ore fluid in different parts of the system. In
296 hydrothermal fluids, Sb^{3+} may be transported mainly as thioantimonite ($H_2Sb_2S_4$, $HSb_2S_4^-$,
297 $Sb_2S_4^{2-}$), hydroxothioantimonite ($Sb_2S_2(OH)_2$), hydroxide ($Sb(OH)_3$, $Sb(OH)_4^-$), and chloride
298 ($SbCl_3$, $SbCl_4^-$, and $SbCl_5^{2-}$) complexes (Krupp, 1988; Williams-Jones and Norman, 1997;
299 Hagemann and Luders, 2003). Previous studies of the Xikuangshan deposit reported that Sb
300 mineralization precipitated from a hydrothermal fluid with a salinity of 0.2-14.8 wt.% NaCl
301 equiv., and a slightly acidic to neutral pH (~5.5-6.5) over the temperature range 105-305 °C
302 (Lin, 2014; Hu and Peng, 2018; Zhang, 2018). For a hydrothermal fluid at those conditions,
303 thermodynamic calculations indicate that the dominant Sb complexes in the fluid are
304 $H_2Sb_2S_4$ and $Sb_2S_2(OH)_2$ (Fig. 6C). Although their associated isotope fractionations are
305 poorly understood, heavier isotope (^{123}Sb) is preferentially partitioned into the site with the
306 highest bond energy, which is demonstrated for many systems (Penniston-Dorland et al.,
307 2017). Bond energies of Sb-H (56.4 kcal/mol), Sb-S (90.5 kcal/mol), and Sb-O (102.8
308 kcal/mol) increase in turn (Luo, 2005), indicating that ^{123}Sb is preferentially complexed as
309 Sb-O, then Sb-S, and finally Sb-H during precipitation of stibnite (Sb_2S_3) from the
310 hydrothermal fluid. The Rayleigh fractionation model results reported here (Fig. 6B)
311 indicate that ^{123}Sb is preferentially partitioned into stibnite, indicating the dominant Sb
312 complex is $H_2Sb_2S_4$ in the fluid responsible for mineralization in the steeply-dipping
313 orebody, whereas ^{121}Sb is preferentially partitioned into stibnite in the shallowly-dipping

orebody indicating the dominant Sb complex is $Sb_2S_2(OH)_2$ in the fluid responsible for mineralization in the shallowly-dipping orebody.

Precipitation of stibnite from an $H_2Sb_2S_4$-bearing fluid in the steeply-dipping orebody would follow a decrease in activity of H_2S (aH_2S) in the fluid, as shown by the following equation from Krupp (1988):

$$H_2Sb_2S_4 = Sb_2S_3 + H_2S \quad (3)$$

Boiling and wall rock sulfidation are major mechanisms to decrease the aH_2S. The modally-minor amount of pyrite and arsenopyrite in the host rock at Xikuangshan rule out the possibility of wall rock sulfidation. Thus, the most likely mechanism of ore precipitation in the steeply-dipping orebodies was fluid boiling, which could have occurred by dramatic pressure fluctuations through both localized fracture dilation and fluid ascent along the major fault (Fig. 7; Voisey et al., 2020). Notably, as aH_2S decreases, $Sb_2S_2(OH)_2$ becomes the dominant stable Sb complex in the fluid (path from point 1 through 2 in Fig. 6C), wherein ^{121}Sb is preferentially partitioned into stibnite as it crystallizes from the fluid. Precipitation of stibnite from the ore fluid can be described by the reaction:

$$Sb_2S_2(OH)_2 + H_2S = Sb_2S_3 + 2H_2O \quad (4)$$

which indicates that decreasing the aH_2S does not decrease the concentration of Sb in the fluid but rather shifts the fluid-stable Sb complex to $Sb_2S_2(OH)_2$. Therefore, the most plausible precipitation mechanism for the shallowly-dipping orebodies is a decrease in temperature (path from point 2 through 3 in Fig. 6C). Cooling of the hypogene ore fluid can occur by bringing deeply sourced fluids into colder wall rock or mixing with meteoric waters. Published fluid inclusion data and H-O isotope data of quartz veins coeval with stibnite indicate that meteoric and pore fluids was present in the host rocks for the

337 shallowing dipping orebodies prior to infiltration of the Sb-bearing ore fluid (Hu and Peng,
338 2018). This means that the fluid mixing with meteoric and pore fluids would have resulted
339 in cooling of the ore fluid and precipitation of stibnite in the shallowly-dipping orebodies
340 with the range of δ^{123}Sb values reported here (Figs. 6C, 7).
341
342 **7. Implications**
343 Transition of the dominant Sb complex from thioantimonite ($H_2Sb_2S_4$) to
344 hydroxothioantimonite ($Sb_2S_2(OH)_2$) in hydrothermal fluids occurs with consuming of H_2S.
345 The initial dominant Sb complex maybe $H_2Sb_2S_4$ in hydrothermal fluids. In this stage,
346 boiling of the ore fluid inducing a decrease in H_2S that reduced the solubility of $H_2Sb_2S_4$ is
347 the main precipitation mechanism. Meanwhile, ^{123}Sb is preferentially complexed as Sb-S,
348 showing a systematical decrease in δ^{123}Sb values. As consuming of H_2S, $Sb_2S_2(OH)_2$
349 becomes the dominant stable Sb complex in the fluid, wherein ^{121}Sb is preferentially
350 partitioned into stibnite as it crystallizes from the fluid. Precipitation of stibnite from the ore
351 fluid is triggered by fluid cooling. Our work shows that stable metal complex in the
352 hydrothermal ore fluid may change induced by fluid evolution and affect the isotope
353 fractionation and metal precipitation mechanisms.
354
355 **Acknowledgements**
356 This research was financially supported by the National Natural Science Foundation of
357 China (42072087, 42130801), the Beijing Nova Program (Z201100006820097), and the 111
358 Project of the Ministry of Science and Technology (BP0719021). Adam C. Simon
359 acknowledges support from NSF EAR #1924192. We thank the anonymous reviewers and

Associate Editor William Peck for their constructive reviews, which helped improve the quality of this paper.

References

Deng, J., Wang, Q., and Li, G. (2017) Tectonic evolution, superimposed orogeny, and composite metallogenic system in China. Gondwana Research, 50, 216–266.

Deng, J., and Wang, Q.F. (2016) Gold mineralization in China: Metallogenic provinces, deposit types and tectonic framework. Gondwana Research, 36, 219–274.

Deng, J., Wang, Q.F., Santosh, M., Liu, X.F., Liang, Y.Y., Yang, L.Q., Zhao, R., and Yang, L. (2020a) Remobilization of metasomatized mantle lithosphere: a new model for the Jiaodong gold province, eastern China. Mineralium Deposita, 55(2), 257-274.

Deng, J., Yang, L.Q., Groves, D.I., Zhang, L., Qiu, K.F., and Wang, Q.F. (2020b) An integrated mineral system model for the gold deposits of the giant Jiaodong province, eastern China. Earth-Science Reviews, 208, 103274.

Deng, J., Zhai, Y., Mo, X., and Wang, Q. (2019) Temporal-spatial distribution of metallic ore deposits in China and their geodynamic settings. Society of Economic Geologists, 22, 103–132.

Fu, S.L., Hu, R.Z., Batt, G.E., Danišík, M., Evans, N.J., and Mi, X.F. (2020a) Zircon (U-Th)/He thermochronometric constraints on the mineralization of the giant Xikuangshan Sb deposit in central Hunan, South China. Mineralium Deposita, 55(5), 901–912.

Fu, S.L., Hu, R.Z., Peng, J.T., Wu, L.Y., and Ma, D.S. (2022) A comprehensive genetic model for the world's largest Sb deposit (Xikuangshan, China). Geological Society of

383 America Bulletin.
384 Fu, S.L., Hu, R.Z., Yin, R.S., Yan, J., Mi, X.F., Song, Z.C., and Sullivan, N. (2020b)
385 Mercury and in situ sulfur isotopes as constraints on the metal and sulfur sources for
386 the world's largest Sb deposit at Xikuangshan, southern China. Mineralium Deposita,
387 55, 1353–1364.
388 Fu, S.L., Lan, Q., and Yan, J. (2020c) Trace element chemistry of hydrothermal quartz and
389 its genetic significance: A case study from the Xikuangshan and Woxi giant Sb
390 deposits in southern China. Ore Geology Reviews, 126, 103732.
391 Fu, S.L., Zajacz, Z., Tsay, A., and Hu, R.Z. (2020d) Can magma degassing at depth donate
392 the metal budget of large hydrothermal Sb deposits? Geochimica et Cosmochimica
393 Acta, 290, 1–15.
394 Gao, Z.F., Zhu, X.K., Sun, J., Luo, Z.H., Bao, C., Tang, C., and Ma, J.X. (2018) Spatial
395 evolution of Zn-Fe-Pb isotopes of sphalerite within a single ore body: A case study
396 from the Dongshengmiao ore deposit, Inner Mongolia, China. Mineralium Deposita,
397 53(1), 55–65.
398 Goldfarb, R.J., Qiu, K.F., Deng, J., Chen, Y.J., and Yang, L.Q. (2019) Orogenic gold
399 deposits of China. In Z.S. Chang, and R.J. Goldfarb, Eds. Mineral Deposies of
400 China, p. 263–324. Society of Economic Geologists, Inc., Kansas.
401 Gregory, M.J., and Mathur, R. (2017) Understanding Copper Isotope Behavior in the High
402 Temperature Magmatic-Hydrothermal Porphyry Environment. Geochemistry
403 Geophysics Geosystems, 18(11), 4000–4015.
404 Hagemann, S.G., and Luders, V. (2003) PTX conditions of hydrothermal fluids and
405 precipitation mechanism of stibnite-gold mineralization at the Wiluna lode-gold

406 deposits, Western Australia: conventional and infrared microthermometric
407 constraints. Mineralium Deposita, 38(8), 936–952.
408 Hannah, J.L., Stein, H.J., Wieser, M.E., de Laeter, J.R., and Varner, M.D. (2007)
409 Molybdenum isotope variations in molybdenite: Vapor transport and Rayleigh
410 fractionation of Mo. Geology, 35(8), 703–706.
411 Hofstra, A.H., Marsh, E.E., Todorov, T.I., and Emsbo, P. (2013) Fluid inclusion evidence
412 for a genetic link between simple antimony veins and giant silver veins in the Coeur
413 d'Alene mining district, ID and MT, USA. Geofluids, 13(4), 475–493.
414 Hu, A.X., and Peng, J.T. (2018) Fluid inclusions and ore precipitation mechanism in the
415 giant Xikuangshan mesothermal antimony deposit, South China: Conventional and
416 infrared microthermometric constraints. Ore Geology Reviews, 95, 49–64.
417 Hu, R.Z., Fu, S.L., Huang, Y., Zhou, M.F., Fu, S.H., Zhao, C.H., Wang, Y.J., Bi, X.W., and
418 Xiao, J.F. (2017) The giant South China Mesozoic low-temperature metallogenic
419 domain: Reviews and a new geodynamic model. Journal of Asian Earth Sciences,
420 137, 9–34.
421 Kaufmann, A.B., Lazarov, M., Kiefer, S., Majzlan, J., and Weyer, S. (2021) In situ
422 determination of antimony isotope ratios in Sb minerals by femtosecond LA-MC-
423 ICP-MS. Journal of Analytical Atomic Spectrometry, 36(7), 1554–1567.
424 Kelley, K., Wilkinson, J., Chapman, J., Crowther, H., and Weiss, D. (2009) Zinc isotopes in
425 sphalerite from base metal deposits in the Red Dog district, northern Alaska.
426 Economic Geology, 104(6), 767–773.
427 Kendall, B., Dahl, T.W., and Anbar, A.D. (2017) Good Golly, Why Moly? The Stable
428 Isotope Geochemistry of Molybdenum. In F.Z. Teng, J. Watkins, and N. Dauphas,

Eds. Non-Traditional Stable Isotopes, 82, p. 683–732. Mineralogical Soc Amer & Geochemical Soc, Chantilly.

Krupp, R. (1988) Solubility of stibnite in hydrogen sulfide solutions, speciation, and equilibrium constants, from 25 to 350 C. Geochimica et Cosmochimica Acta, 52(12), 3005–3015.

Li, Y., McCoy, W., Alex J, Zhang, S., Selby, D., Burton, K.W., and Horan, K. (2019) Controlling mechanisms for molybdenum isotope fractionation in porphyry deposits: the Qulong example. Economic Geology, 114(5), 981–992.

Lin, F.M. (2014) On the ore-forming fluid in the Xikuangshan antimony deposit, Central Hunan, Master, p. 70. Central South University, Changsha.

Lobo, L., Devulder, V., Degryse, P., and Vanhaecke, F. (2012) Investigation of natural isotopic variation of Sb in stibnite ores via multi-collector ICP-mass spectrometry – perspectives for Sb isotopic analysis of Roman glass. Journal of Analytical Atomic Spectrometry, 27(8).

Long, Z.Y., Qiu, K.F., Santosh, M., Yu, H.C., Jiang, X.Y., Zou, L.Q., and Tang, D.W. (2022) Fingerprinting the metal source and cycling of the world's largest antimony deposit in Xikuangshan, China. GSA Bulletin.

Luo, K., Zhou, J.X., Feng, Y.X., Uysal, I.T., Nguyen, A., Zhao, J.X., and Zhang, J. (2020) In situ U-Pb dating of calcite from the South China antimony metallogenic belt. Iscience, 23(10), 101575.

Luo, Y.R. (2005) Handbook of Bond Dissociation. In Y.R. Luo, Ed. Science Press.

Mathur, R., Arribas, A., Megaw, P., Wilson, M., Stroup, S., Meyer-Arrivillaga, D., and Arribas, I. (2018) Fractionation of silver isotopes in native silver explained by redox

452 reactions. Geochimica et Cosmochimica Acta, 224, 313–326.
453 Mathur, R., Ruiz, J., Titley, S., Liermann, L., Buss, H., and Brantley, S. (2005) Cu isotopic
454 fractionation in the supergene environment with and without bacteria. Geochimica
455 Et Cosmochimica Acta, 69(22), 5233–5246.
456 Mondillo, N., Wilkinson, J.J., Boni, M., Weiss, D.J., and Mathur, R. (2018) A global
457 assessment of Zn isotope fractionation in secondary Zn minerals from sulfide and
458 non-sulfide ore deposits and model for fractionation control. Chemical Geology, 500,
459 182–193.
460 Moynier, F., Vance, D., Fujii, T., and Savage, P. (2017) The Isotope Geochemistry of Zinc
461 and Copper. In F.Z. Teng, J. Watkins, and N. Dauphas, Eds. Non-Traditional Stable
462 Isotopes, 82, p. 543–600. Mineralogical Soc Amer & Geochemical Soc, Chantilly.
463 Muntean, J.L., Cline, J.S., Simon, A.C., and Longo, A.A. (2011) Magmatic–hydrothermal
464 origin of Nevada's Carlin-type gold deposits. Nature Geoscience, 4(2), 122–127.
465 Neyedley, K., Hanley, J.J., Fayek, M., and Kontak, D.J. (2017) Textural, Fluid Inclusion,
466 and Stable Oxygen Isotope Constraints on Vein Formation and Gold Precipitation at
467 the 007 Deposit, Rice Lake Greenstone Belt, Bissett, Manitoba, Canada. Economic
468 Geology, 112, 629–660.
469 Ohmoto, H. (2018) Stable isotople geochemistry of ore deposits In W.V. John, P.T. Hugh,
470 and R.O.N. James, Eds. Stable Isotopes in High Temperature Geological Processes, p.
471 491–560. De Gruyter.
472 Penniston-Dorland, S., Liu, X.M., and Rudnick, R. (2017) Lithium isotope geochemistry.
473 Reviews in Mineralogy, 82(1), 165–217.
474 Qiu, K.F., Marsh, E., Yu, H.C., Pfaff, K., Gulbransen, C., Gou, Z.Y., and Li, N. (2017)

475 Fluid and metal sources of the Wenquan porphyry molybdenum deposit, Western
476 Qinling, NW China. Ore Geology Reviews, 86, 459–473.
477 Qiu, K.F., Yu, H.C., Deng, J., McIntire, D., Gou, Z.Y., Geng, J.Z., Chang, Z.S., Zhu, R., Li,
478 K.N., and Goldfarb, R. (2020) The giant Zaozigou Au-Sb deposit in West Qinling,
479 China: magmatic- or metamorphic-hydrothermal origin? Mineralium Deposita, 55(2),
480 345–362.
481 Qiu, K.F., Yu, H.C., Hetherington, C., Huang, Y.Q., Yang, T., and Deng, J. (2021)
482 Tourmaline composition and boron isotope signature as a tracer of magmatic-
483 hydrothermal processes. American Mineralogist, 106(7), 1033–1044.
484 Resongles, E., Freydier, R., Casiot, C., Viers, J., Chmeleff, J., and Elbaz-Poulichet, F. (2015)
485 Antimony isotopic composition in river waters affected by ancient mining activity.
486 Talanta, 144, 851–861.
487 Rouxel, O., Ludden, J., and Fouquet, Y. (2003) Antimony isotope variations in natural
488 systems and implications for their use as geochemical tracers. Chemical Geology,
489 200(1-2), 25–40.
490 Schulz, K.J., DeYoung, J.H., Seal, R.R., and Bradley, D.C. (2018) Critical mineral resources
491 of the United States: economic and environmental geology and prospects for future
492 supply. U.S.Geological Survey.
493 Su, W., Heinrich, C.A., Pettke, T., Zhang, X., Hu, R., and Xia, B. (2009) Sediment-Hosted
494 Gold Deposits in Guizhou, China: Products of Wall-Rock Sulfidation by Deep
495 Crustal Fluids. Economic Geology, 104(1), 73–93.
496 Tanimizu, M., Araki, Y., Asaoka, S., and Takahashi, Y. (2011) Determination of natural
497 isotopic variation in antimony using inductively coupled plasma mass spectrometry

498 for an uncertainty estimation of the standard atomic weight of antimony.
499 Geochemical Journal, 45(1), 27–32.
500 Teng, F.Z. (2017) Magnesium Isotope Geochemistry. In F.Z. Teng, J. Watkins, and N.
501 Dauphas, Eds. Non-Traditional Stable Isotopes, 82, p. 219–287. Mineralogical Soc
502 Amer & Geochemical Soc, Chantilly.
503 Toutain, J.P., Sonke, J., Munoz, M., Nonell, A., Polv, M., Viers, J.m., Freydier, R., Sortino,
504 F., Joron, J.L., and Sumarti, S. (2008) Evidence for Zn isotopic fractionation at
505 Merapi volcano. Chemical Geology, 253(1-2), 74–82.
506 Voisey, C.R., Tomkins, A.G., and Xing, Y. (2020) Analysis of a Telescoped Orogenic Gold
507 System: Insights from the Fosterville Deposit. Economic Geology, 115(8), 1645–
508 1664.
509 Wang, D., Zheng, Y., Mathur, R., and Yu, M. (2020a) Fractionation of cadmium isotope
510 caused by vapour-liquid partitioning in hydrothermal ore-forming system: A case
511 study of the Zhaxikang Sb-Pb-Zn-Ag deposit in Southern Tibet. Ore Geology
512 Reviews, 119, 103400.
513 Wang, D., Zheng, Y.Y., Mathur, R., and Wu, S. (2018) The Fe-Zn Isotopic Characteristics
514 and Fractionation Models: Implications for the Genesis of the Zhaxikang Sb-Pb-Zn-
515 Ag Deposit in Southern Tibet. Geofluids, 2197891.
516 Wang, Q.F., Yang, L., Xu, X.J., Santosh, M., Wang, Y.N., Wang, T.Y., Chen, F.G., Wang,
517 R.X., Gao, L., Liu, X.F., Yang, S.J., Zeng, Y.S., Chen, J.H., Zhang, Q.Z., and Deng,
518 J. (2020b) Multi-stage tectonics and metallogeny associated with Phanerozoic
519 evolution of the South China Block: A holistic perspective from the Youjiang Basin.
520 Earth-Science Reviews, 211.

Watkins, J.M., DePaolo, D.J., and Watson, E.B. (2017) Kinetic Fractionation of Non-Traditional Stable Isotopes by Diffusion and Crystal Growth Reactions. In F.Z. Teng, J. Watkins, and N. Dauphas, Eds. Non-Traditional Stable Isotopes, 82, p. 85–125. Mineralogical Soc Amer & Geochemical Soc, Chantilly.

Wen, B., Zhou, J., Zhou, A., Liu, C., and Li, L. (2018) A review of antimony (Sb) isotopes analytical methods and application in environmental systems. International Biodeterioration & Biodegradation, 128, 109–116.

Wen, H.J., Zhu, C.W., Zhang, Y.X., Cloquet, C., Fan, H.F., and Fu, S.H. (2016) Zn/Cd ratios and cadmium isotope evidence for the classification of lead-zinc deposits. Scientific Reports, 6.

Williams-Jones, A.E., and Norman, C. (1997) Controls of mineral parageneses in the system Fe-Sb-SO. Economic Geology, 92(3), 308–324.

Wilson, N., Webster-Brown, J., and Brown, K. (2007) Controls on stibnite precipitation at two New Zealand geothermal power stations. Geothermics, 36(4), 330–347.

Wu, L.S., and Hu, X.W. (2000) Xikuangshan mica-plagioclase lamprophyre and its granite inclusions, Hunan Province. Geology-Geochemistry, 28, 51–55.

Wu, M., Samson, I.M., Qiu, K., and Zhang, D. (2021) Concentration Mechanisms of Rare Earth Element-Nb-Zr-Be Mineralization in the Baerzhe Deposit, Northeast China: Insights from Textural and Chemical Features of Amphibole and Rare Metal Minerals. Economic Geology, 116(3), 651-679.

Xie, G.Q., Peng, J.T., Hu, R.Z., and Jia, D.C. (2001) Geochemical characteristics of lamprophyres in the Xikuangshan antimony ore deposits, Hunan province. Acta Petrologica Sinica, 17, 629–636.

544 Xie, Z. (2018) Are There Carlin-Type Gold Deposits in China? A Comparison of the
545 Guizhou, China, Deposits with Nevada, USA, Deposits. In J.L. Muntean, Ed.
546 Diversity in Carlin-Style Gold Deposits, p. 187–233.
547 Yan, J., Fu, S., Liu, S., Wei, L., and Wang, T. (2022) Giant Sb metallogenic belt in South
548 China: A product of Late Mesozoic flat-slab subduction of paleo-Pacific plate. Ore
549 Geology Reviews, 142, 104697.
550 Yang, R.Y., Ma, D.S., Bao, Z.Y., Pan, J.Y., Cao, S.L., and Xia, F. (2006) Geothermal and
551 fluid flowing simulation of ore-forming antimony deposits in Xikuangshan. Science
552 in China Series D-Earth Sciences, 49(8), 862–871.
553 Yu, H.C., Qiu, K.F., Deng, J., Zhu, R., Mathieu, L., Sai, S.X., and Sha, W.J. (2022)
554 Exhuming and preserving epizonal orogenic Au-Sb deposits in rapidly uplifting
555 orogenic settings. Tectonics, 41, 2021TC007165.
556 Yu, H.C., Qiu, K.F., Hetherington, C.J., Chew, D., Huang, Y.Q., He, D.Y., Geng, J.Z., and
557 Xian, H.Y. (2021) Apatite as an alternative petrochronometer to trace the evolution
558 of magmatic systems containing metamict zircon. Contributions to Mineralogy and
559 Petrology, 176(9), 86.
560 Yu, H.C., Qiu, K.F., Nassif, M.T., Geng, J.Z., Sai, S.X., Duo, D.W., Huang, Y.Q., and
561 Wang, J. (2020) Early orogenic gold mineralization event in the West Qinling related
562 to closure of the Paleo-Tethys Ocean-Constraints from the Ludousou gold deposit,
563 central China. Ore Geology Reviews, 117, 103217.
564 Zhai, D., Mathur, R., Liu, S., Liu, J., Godfrey, L., Wang, K., Xu, J., and Vervoort, J. (2021)
565 Antimony isotope fractionation in hydrothermal systems. Geochimica et
566 Cosmochimica Acta, 84–97.

Zhang, L., Qiu, K., Hou, Z., Pirajno, F., Shivute, E., and Cai, Y. (2021) Fluid-rock reactions of the Triassic Taiyangshan porphyry Cu-Mo deposit (West Qinling, China) constrained by QEMSCAN and iron isotope. Ore Geology Reviews, 132, 104068.

Zhang, T.Y., Li, C.Y., Sun, S.J., and Hao, X.L. (2020) Geochemical characteristics of antimony and genesis of antimony deposits in South China. Acta Petrologica Sinica, 36(1), 44–54.

Zhang, Y. (2018) Ore-forming fluid evolution and Sb-Au-W metallogensis in the Central Hunan-Northwestern Jiangxi, South China, Doctor, p. 161. Nanjing University, Nanjing.

Zhu, C.W., Wen, H.J., Zhang, Y.X., Fu, S.H., Fan, H.F., and Cloquet, C. (2017) Cadmium isotope fractionation in the Fule Mississippi Valley-type deposit, Southwest China. Mineralium Deposita, 52(5), 675–686.

Zhu, Z.Y., Jiang, S.Y., Mathur, R., Cook, N.J., Yang, T., Wang, M., Ma, L., and Ciobanu, C.L. (2018) Iron isotope behavior during fluid/rock interaction in K-feldspar alteration zone-A model for pyrite in gold deposits from the Jiaodong Peninsula, East China. Geochimica et Cosmochimica Acta, 222, 94–116.

Zotov, A., Shikina, N., and Akinfiev, N. (2003) Thermodynamic properties of the Sb (III) hydroxide complex Sb (OH)3 (aq) at hydrothermal conditions. Geochimica et Cosmochimica Acta, 67(10), 1821–1836.

Figure captions

588 Fig. 1. Map showing the global distribution of representative antimony deposits. Modified
589 after Deng et al. (2019) and Zhang et al. (2020).
590 Fig. 2. (A) Geological map of the world's largest Sb deposit in Xikuangshan (modified from
591 Fu et al., 2020b). (B) Cross section map of No. 41 exploration line (A-B) showing two types
592 of orebodies (modified from Zhai et al., 2021; Long et al., 2022)
593 Fig. 3. Underground exposures showing the Sb orebody hosted in the silicified limestone.
594 Antimony occurs chiefly as the stibnite from the quartz-stibnite vein (A, B) and calcite-
595 quartz-stibnite vein (C, D).
596 Fig. 4. Silicified limestone (A), euhedral stibnite in limestone (B), stibnite-quartz vein ore
597 (C) and stibnite-calcite-quartz vein ore (D).
598 Fig. 5. Mineral assemblages of the Sb ores. Anhedral stibnite along the margin of the quartz
599 and calcite (A-C) and euhedral needle-shaped crystals in calcite grains (D). Cal = calcite, Stb
600 = stibnite, Qz = quartz.
601 Fig. 6 (A) Schematic cross-section showing sample locations from this work and Zhai et al.
602 (2021). Note that the orebodies of the Xikuangshan deposit show a southward plunge,
603 inducing a relatively deeper mining depth in the southern part of the deposit. As a result, the
604 elevations of the samples represent positions projected on the cross-section rather than the
605 real elevations. (B) The Sb isotopic Rayleigh distillation model of the steeply-dipping and
606 shallowly-dipping orebodies of the Xikuangshan Sb deposit. The grey dots are from Zhai et
607 al. (2021). The initial δ^{123}Sb values of the hydrothermal fluid is defined to 0.530 ‰. The
608 fractionation factors (α_1 for steeply-dipping orebodies and α_2 for shallowly-dipping
609 orebodies) between stibnite and solution are 1.00043 and 0.99978. The δ^{123}Sb values of
610 stibnite change abruptly at the transitional zone. F means the fraction of reactant remaining.

This is the peer-reviewed, final accepted version for American Mineralogist, published by the Mineralogical Society of America.
The published version is subject to change. Cite as Authors (Year) Title. American Mineralogist, in press.
DOI: https://doi.org/10.2138/am-2022-8490. http://www.minsocam.org/

611 (C) Speciation diagram of aqueous Sb species in hydrothermal fluids with superimposed Sb
612 fluid solubility contours. Bold lines indicate boundaries between aqueous Sb species. Circled
613 numbers indicate hypothetical points for illustrating fluid property changes. Superimposed
614 Sb fluid solubility contours of aqueous Sb species in hydrothermal fluids are from
615 Hagemann and Luders (2003).

616 Fig. 7. A schematic cartoon showing telescoped stibnite precipitation mechanisms steeply-
617 dipping and shallowly-dipping orebodies.

618

619 **Table caption**

620 **Table 1** The δ^{123}Sb values of the steeply-dipping and shallowly-dipping orebodies of the
621 Xikuangshan Sb deposit.

No.	Sample No.	Mineral assemblage	Elevation	Weight	Batch	δ^{123}Sb	2 σ (abs)	δ^{123}Sb (repeat)	2 σ (abs)
South Ore Block									
Steeply-dipping orebodies									
1	XKS22	Stb-Cal-Qz	-604 m	0.06 g	1	0.927 ‰	0.03 ‰	0.930 ‰	0.03 ‰
2	XKS23	Stb-Cal-Qz	-604 m	0.06 g	1	0.988 ‰	0.03 ‰	0.956 ‰	0.03 ‰
3	XKS19	Stb-Qz-Cal	-468 m	0.2 g	1	0.798 ‰	0.03 ‰	0.816 ‰	0.03 ‰
4	XKS20	Cal-Qz-Stb	-468 m	1.0 g	1	0.766 ‰	0.03 ‰	0.753 ‰	0.03 ‰
5	XKS21	Qz-Cal-Stb	-468 m	0.04 g	1	0.737 ‰	0.03 ‰	-	-
6	XKS24	Stb-Cal-Qz	-468 m	0.1 g	1	0.753 ‰	0.03 ‰	0.743 ‰	0.03 ‰
7	XKS25	Qz-Cal-Stb	-468 m	0.33 g	1	0.766 ‰	0.03 ‰	-	-
8	XKS26	Cal-Stb	-468 m	0.35 g	2	0.782 ‰	0.03 ‰	-	-
9	XKS12	Stb-Qz-Cal	-192 m	0.5 g	2	0.659 ‰	0.03 ‰	0.666 ‰	0.03 ‰
10	XKS13	Stb-Cal-Qz	-192 m	1.0 g	2	0.578 ‰	0.03 ‰	0.603 ‰	0.03 ‰
11	XKS14	Stb-Cal-Qz	-192 m	0.5 g	2	0.591 ‰	0.03 ‰	0.579 ‰	0.03 ‰

This is the peer-reviewed, final accepted version for American Mineralogist, published by the Mineralogical Society of America.
The published version is subject to change. Cite as Authors (Year) Title. American Mineralogist, in press.
DOI: https://doi.org/10.2138/am-2022-8490. http://www.minsocam.org/

12	XKS15	Stb-Cal-Qz	-192 m	1.0 g	2	0.565 ‰	0.03 ‰	0.552 ‰	0.03 ‰
13	XKS16	Stb-Cal-Qz	-192 m	1.0 g	2	0.523 ‰	0.03 ‰	0.483 ‰	0.03 ‰
14	XKS17	Stb-Qz-Cal	-192 m	0.25 g	1	0.637 ‰	0.03 ‰	0.663 ‰	0.03 ‰
15	XKS18	Qz-Cal-Stb	-192 m	0.03 g	1	0.577 ‰	0.03 ‰	0.574 ‰	0.03 ‰
16	XKS06	Qz-Cal-Stb	-142 m	1.0 g	2	0.610 ‰	0.03 ‰	0.582 ‰	0.03 ‰
17	XKS07	Cal-Qz-Stb	-142 m	1.2 g	2	0.583 ‰	0.03 ‰	0.578 ‰	0.03 ‰
18	XKS08	Cal-Qz-Stb	-142 m	0.8 g	1	0.535 ‰	0.03 ‰	0.528 ‰	0.03 ‰
19	XKS09	Stb-Qz	-142 m	0.7 g	1	0.572 ‰	0.03 ‰	0.570 ‰	0.03 ‰
20	XKS10	Stb-Qz	-142 m	0.8 g	1	0.514 ‰	0.03 ‰	0.554 ‰	0.03 ‰
21	XKS11	Stb-Qz	-142 m	0.2 g	1	0.541 ‰	0.03 ‰	0.496 ‰	0.03 ‰
22	XKS01	Qz-Cal-Stb	-106 m	0.8 g	2	0.589 ‰	0.03 ‰	0.601 ‰	0.03 ‰
23	XKS02	Cal-Qz-Stb	-106 m	1.0 g	2	0.536 ‰	0.03 ‰	0.503 ‰	0.03 ‰
24	XKS03	Cal-Qz-Stb	-106 m	1.0 g	2	0.514 ‰	0.03 ‰	0.474 ‰	0.03 ‰
25	XKS04	Stb-Cal-Qz	-106 m	1.0 g	2	0.547 ‰	0.03 ‰	0.534 ‰	0.03 ‰
26	XKS05	Cal-Qz-Stb	-106 m	1.0 g	2	0.483 ‰	0.03 ‰	0.470 ‰	0.03 ‰
Shallowly-dipping orebodies									
27	19xkss-47		74 m			0.22 ‰			
28	19xkss-48		74 m			0.21 ‰			
29	19xkss-40		2 m			0.6 ‰			
30	19xkss-42		2 m			0.27 ‰			
31	19xkss-39		-34 m			0.41 ‰			
32	19xkss-37		-34 m			0.5 ‰			
33	19xkss-32		-70 m			0.57 ‰			
34	19xkss-31		-70 m			0.53 ‰			
35	19xkss-25		-106 m			0.45 ‰			
36	19xkss-29		-106 m			0.54 ‰			
37	19xkss-18		-192 m			0.63 ‰			
38	19xkss-15		-192 m			0.75 ‰			
39	19xkss-5		-242 m			0.83 ‰			
40	19xkss-2		-242 m			0.86 ‰			
North Ore Block									
Transitional zones between the steeply-dipping and shallowly-dipping orebodies									
27	19xks-45-1		510 m			0.30 ‰			

28	19xks-45-2	510 m	0.44 ‰
29	19xks-45-3	510 m	0.62 ‰
30	19xks-45-4	510 m	0.61 ‰
31	19xks-45-5	510 m	0.52 ‰
32	19xks-45-6	510 m	0.49 ‰
33	19xks-45-7	510 m	0.45 ‰
Shallowly-dipping orebodies			
48	19xks-33-1	480 m	-0.27 ‰
49	19xks-43	480 m	-0.05 ‰
50	19xks-23	450 m	0.01 ‰
51	19xks-24	450 m	-0.11 ‰
52	19xks-58-1	440 m	-0.11 ‰
53	19xks-58-2	440 m	-0.16 ‰
54	19xks-58-3	440 m	-0.11 ‰
55	19xks-58-4	430 m	-0.07 ‰
56	19xks-58-5	430 m	-0.09 ‰
57	19xks-58-6	430 m	-0.08 ‰
58	19xks-61-1	430 m	0.31 ‰
59	19xks-61-2	430 m	0.43 ‰
60	19xks-61-3	430 m	0.40 ‰
61	19xks-61-4	430 m	0.14 ‰
62	19xks-61-5	430 m	0.42 ‰
63	19xks-61-6	430 m	0.31 ‰
64	19xks-54	420 m	0.70 ‰
65	19xks-52-1	420 m	0.18 ‰

622 The weight is complete amount of the stibnite powder. Samples of transitional zones and

623 shallowly-dipping orebodies are from Zhai et al. (2021).

624

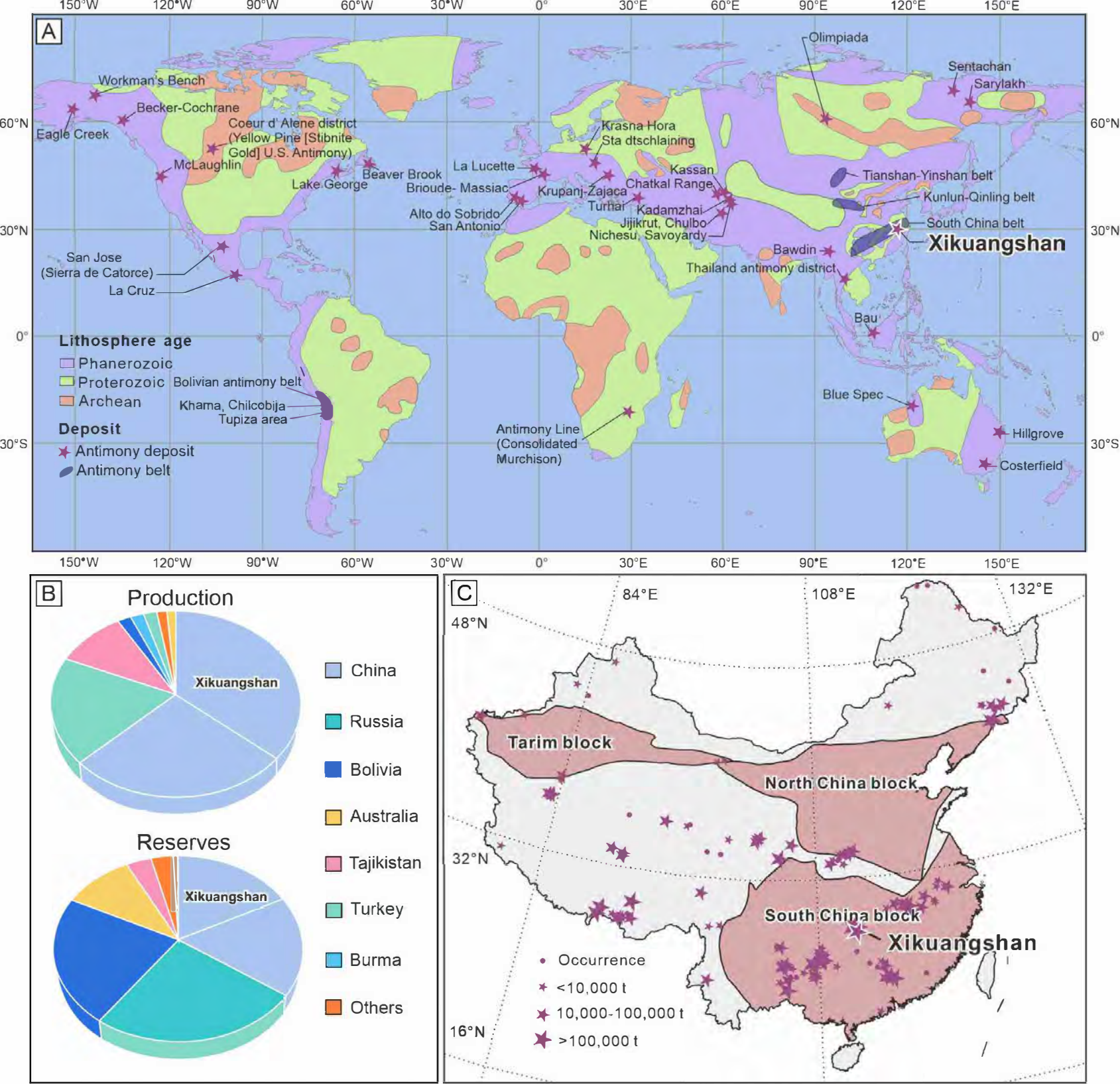
A
Workman's Bench
Becker-Cochrane
Eagle Creek
Coeur d' Alene district
(Yellow Pine [Stibnite
Gold] U.S. Antimony)
McLaughlin
Lake George
Beaver Brook
Brioude- Massiac
La Lucette
Krasna Hora
Sta dtschlaining
Krupanj-Zajaca
Turhal
Alto do Sobrido
San Antonio
Chatkal Range
Kassan
Kadamzhai
Jijikrut, Chulbo
Nichesu, Savoyardy
Olimpiada
Sentachan
Sarylakh
Tianshan-Yinshan belt
Kunlun-Qinling belt
South China belt
Xikuangshan
Bawdin
Thailand antimony district
Bau
Blue Spec
Hillgrove
Costerfield
San Jose
(Sierra de Catorce)
La Cruz
Bolivian antimony belt
Khama, Chilcobija
Tupiza area
Antimony Line
(Consolidated
Murchison)
Lithosphere age
Phanerozoic
Proterozoic
Archean
Deposit
Antimony deposit
Antimony belt
150°W
120°W
90°W
60°W
30°W
0°
30°E
60°E
90°E
120°E
150°E
60°N
30°N
0°
30°S
B
Production
Xikuangshan
Reserves
Xikuangshan
China
Russia
Bolivia
Australia
Tajikistan
Turkey
Burma
Others
C
84°E
108°E
132°E
48°N
32°N
16°N
Tarim block
North China block
South China block
Xikuangshan
Occurrence
<10,000 t
10,000-100,000 t
>100,000 t

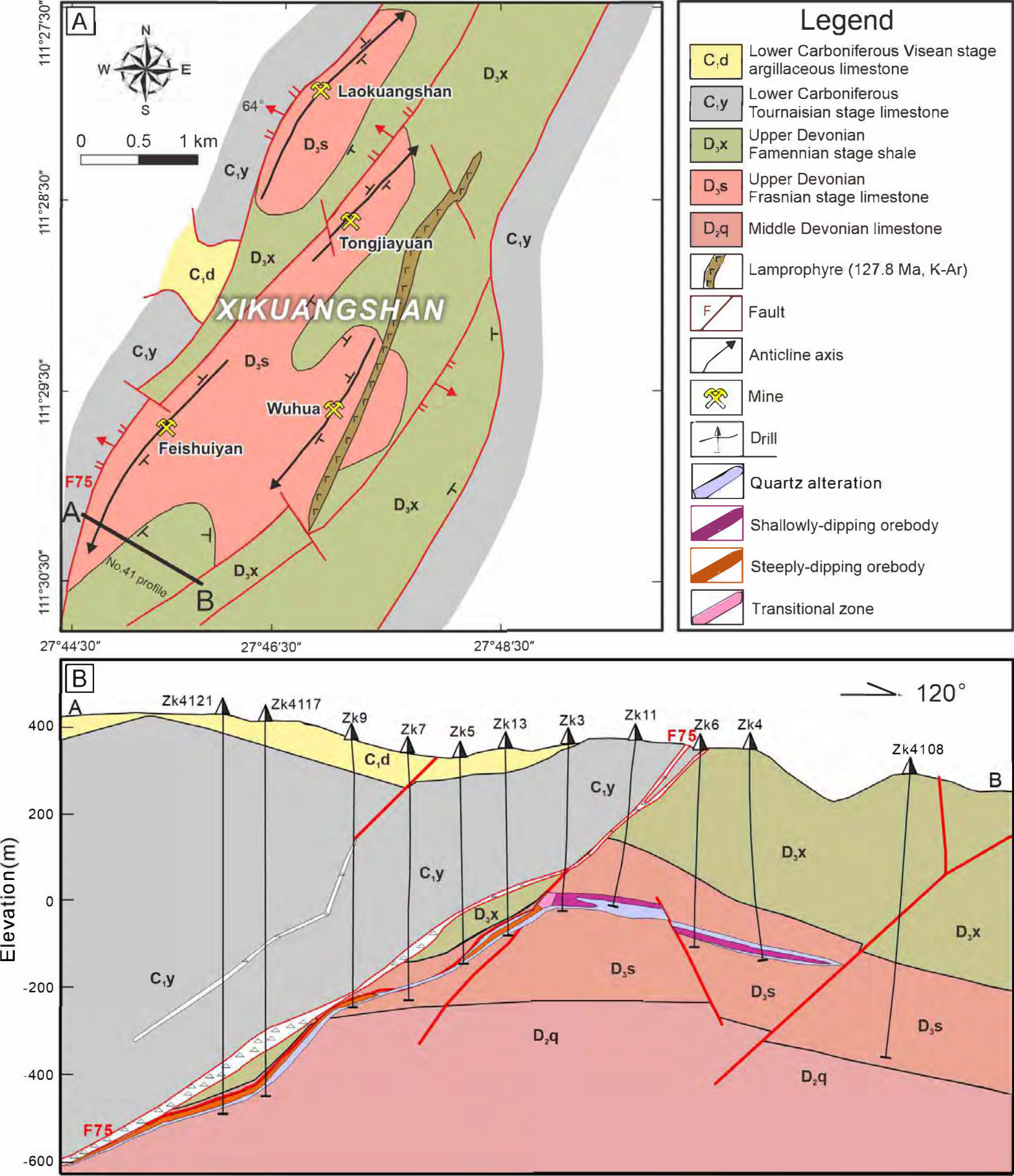
A
N
W
E
S
0 0.5 1 km
64°
Laokuangshan
Tongjiayuan
Wuhua
Feishuiyan
XIKUANGSHAN
F75
No.41 profile
A
B
D_3x
D_3s
C_1y
C_1d
D_2q
111°27′30″
111°28′30″
111°29′30″
111°30′30″
27°44′30″
27°46′30″
27°48′30″
Legend
Lower Carboniferous Visean stage argillaceous limestone
Lower Carboniferous Tournaisian stage limestone
Upper Devonian Famennian stage shale
Upper Devonian Frasnian stage limestone
Middle Devonian limestone
Lamprophyre (127.8 Ma, K-Ar)
Fault
Anticline axis
Mine
Drill
Quartz alteration
Shallowly-dipping orebody
Steeply-dipping orebody
Transitional zone
B
A
B
120°
Zk4121
Zk4117
Zk9
Zk7
Zk5
Zk13
Zk3
Zk11
Zk6
Zk4
Zk4108
F75
Elevation(m)
400
200
0
-200
-400
-600

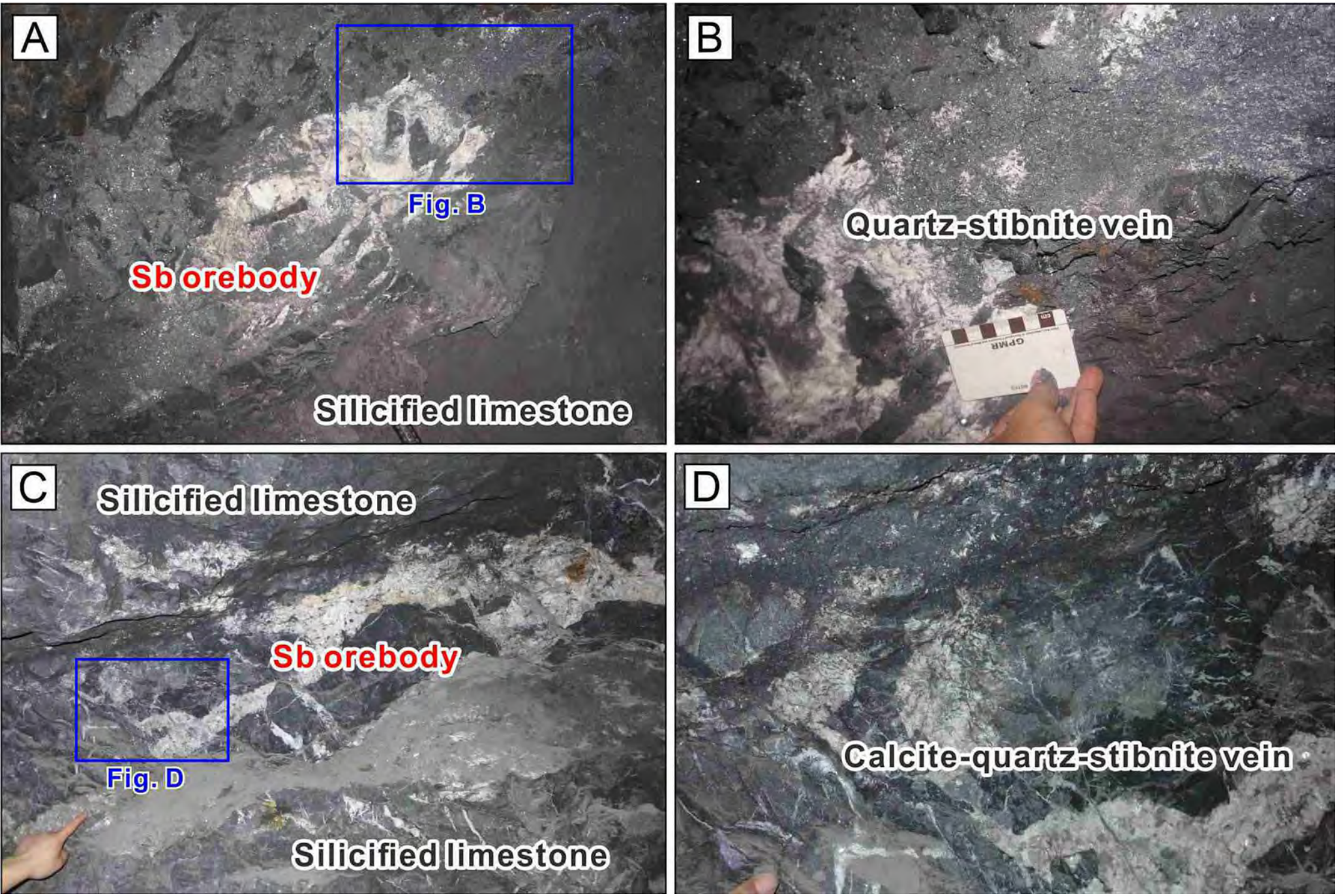
A
Fig. B
Sb orebody
Silicified limestone
B
Quartz-stibnite vein
C
Silicified limestone
Sb orebody
Fig. D
Silicified limestone
D
Calcite-quartz-stibnite vein

A

Silicified limestone

B

Euhedral stibnite in limestone

C

Stibnite-quartz vein

D

Stibnite-calcite-quartz vein

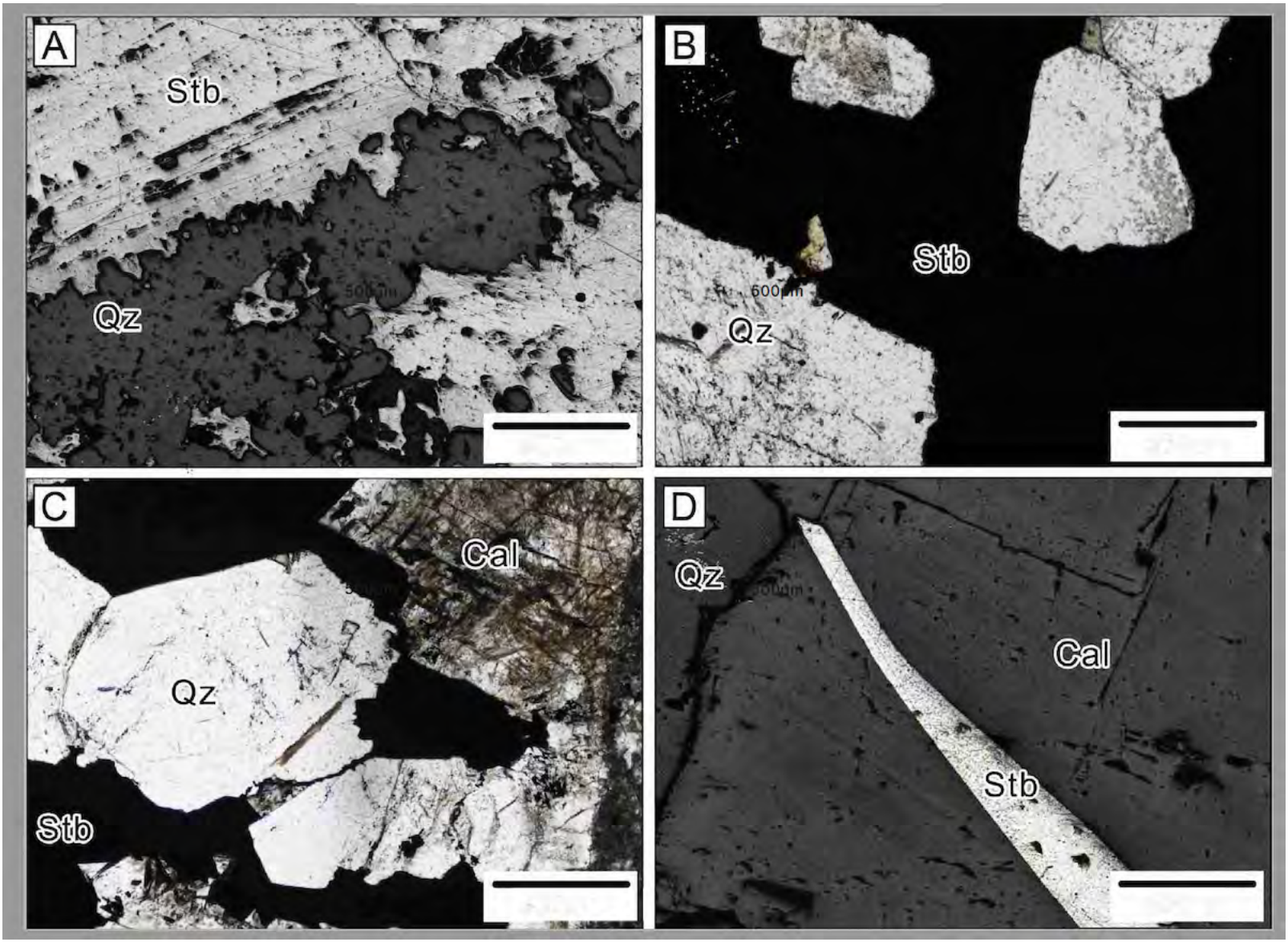
A
Stb
Qz
B
Stb
Qz
C
Cal
Qz
Stb
D
Qz
Cal
Stb

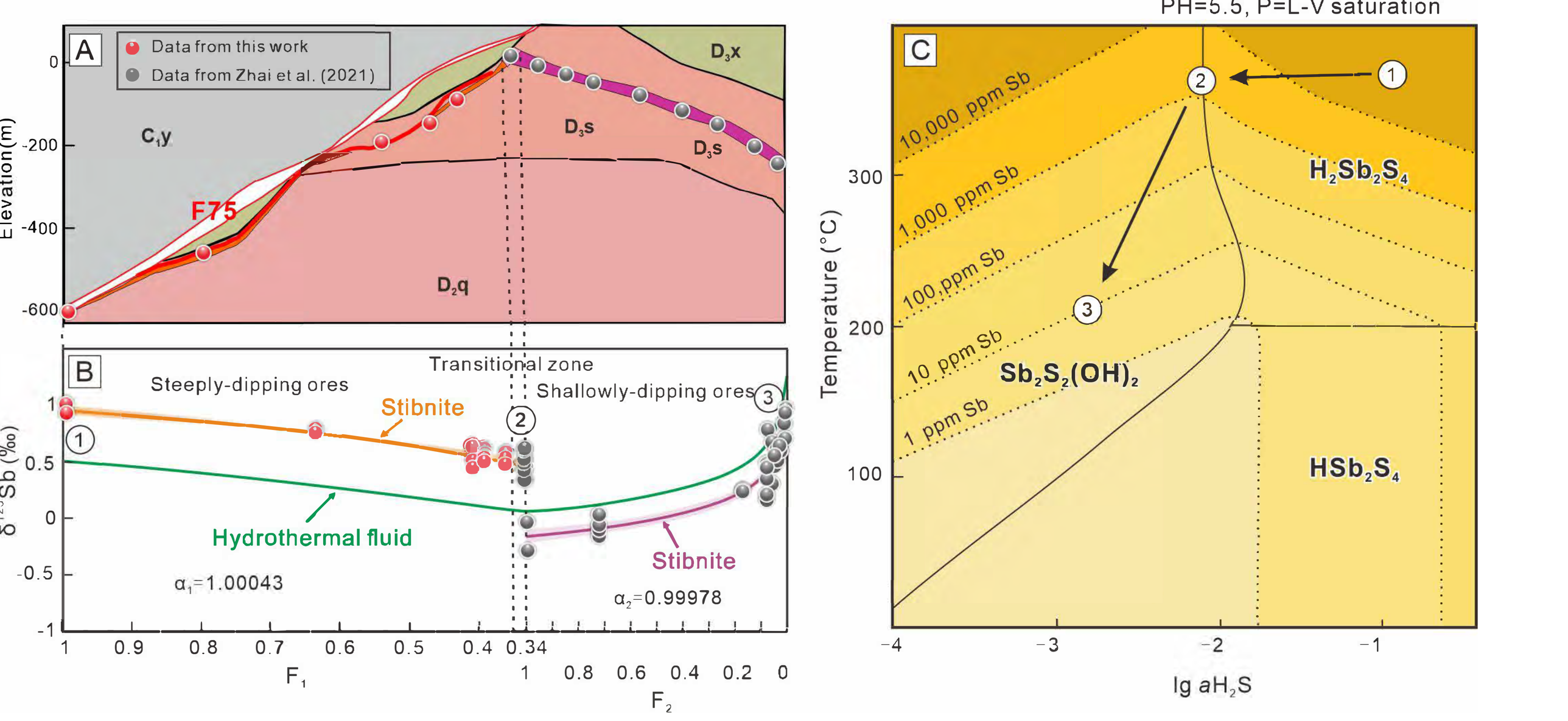
A
Data from this work
Data from Zhai et al. (2021)
Elevation(m)
0
-200
-400
-600
C_1y
D_3x
D_3s
D_3s
F75
D_2q
B
Transitional zone
Steeply-dipping ores
Shallowly-dipping ores
Stibnite
Hydrothermal fluid
Stibnite
α_1=1.00043
α_2=0.99978
δ^{123}Sb (‰)
1
0.5
0
-0.5
-1
1
0.9
0.8
0.7
0.6
0.5
0.4
0.34
F_1
1
0.8
0.6
0.4
0.2
0
F_2
PH=5.5, P=L-V saturation
C
10,000 ppm Sb
1,000 ppm Sb
100 ppm Sb
10 ppm Sb
1 ppm Sb
$H_2Sb_2S_4$
$Sb_2S_2(OH)_2$
HSb_2S_4
Temperature (°C)
300
200
100
−4
−3
−2
−1
lg aH_2S

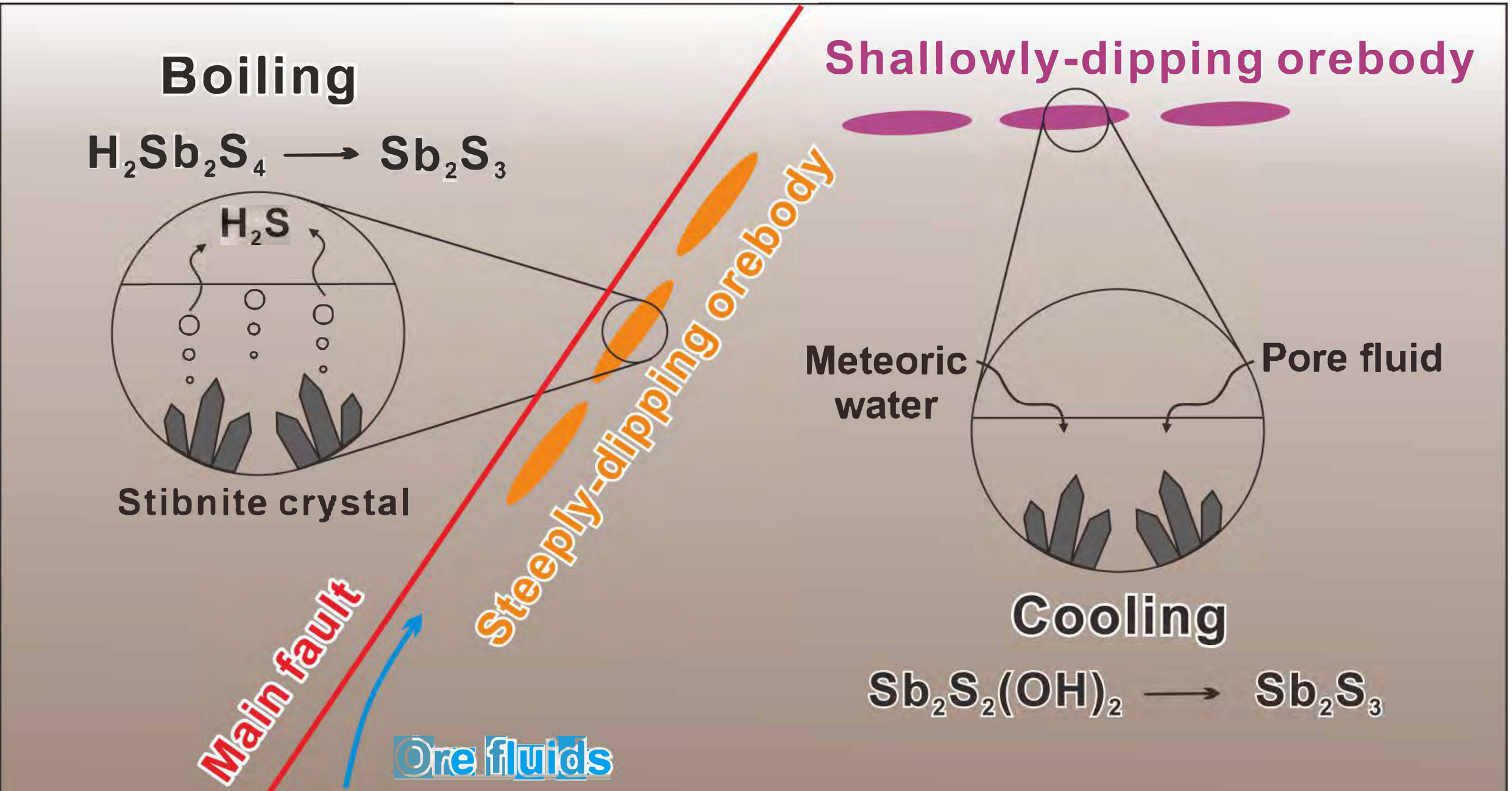
Boiling
$H_2Sb_2S_4 \longrightarrow Sb_2S_3$
H_2S
Stibnite crystal
Main fault
Steeply-dipping orebody
Ore fluids
Shallowly-dipping orebody
Meteoric water
Pore fluid
Cooling
$Sb_2S_2(OH)_2 \longrightarrow Sb_2S_3$